HEART SIMULATION BY AN IMMERSED BOUNDARY METHOD WITH FORMAL SECOND-ORDER ACCURACY AND REDUCED NUMERICAL VISCOSITY

David M. McQueen and Charles S. Peskin
Courant Institute of Mathematical Sciences
New York University, New York, USA
mcqueen@cims.nyu.edu, peskin@cims.nyu.edu

"Although during the past 50 years pure mathematicians have become more and more rigorous, the restraints on applied mathematicians have been, in practice, altogether removed. For instance, P. A. M. Dirac of Cambridge introduced a 'delta function' that has the property of being infinite at one point and zero everywhere else but has a finite integral, and the applied men now make the most reckless use of it without incurring any censure . . . "
—Sir Edmund Whittaker, *Scientific American*, September 1950

Abstract This paper describes a formally second-order accurate version of the immersed boundary method and its application to the computer simulation of blood flow in a three-dimensional model of the human heart.

1. INTRODUCTION

The immersed boundary method [1]–[3] was developed to study flow patterns around heart valves, and is a generally useful method for problems in which elastic material interacts with a viscous incompressible fluid. (The elastic material may have time-dependent elastic parameters, in which case it can contract and relax, like a muscle.) Most problems of biofluid dynamics are of this kind, and the method has been applied to several such problems [2], [4]–[18]. Until recently, however, the immersed boundary method was only first-order accurate.

An immersed boundary method with formal second-order accuracy was introduced in the Ph.D. thesis of Ming-Chih Lai [19]—see also [20].

(The concept of "formal" second-order accuracy will be explained below.) Lai applied this new methodology to the well-known two-dimensional benchmark problem of flow past a cylinder, for which the first-order accurate immersed boundary method typically generates a drag that is too high and a Strouhal number (for vortex shedding) that is too low, each by about 20%, on a typical grid. On the same grid, Lai found that the formally second-order accurate method is in excellent agreement with physical experiments and with other high-precision numerical methods. The improved accuracy was accompanied by a visible improvement in the resolution of vortices shed from the cylinder, which look tighter (less diffuse) than those generated in the corresponding first-order accurate simulation. Taken together, these changes strongly suggest that the main benefit of the formally second-order method is a reduction in numerical viscosity.

Our purpose here is to apply this improved, benchmarked methodology to the heart. This application requires a three-dimensional implementation, which is the main advance reported here, but we have also made a few minor methodological changes along the way, so the method reported in this paper will be slightly different from the one in the Lai references cited above.

Formal second-order accuracy means that the method in question would be second-order accurate if it were applied to a problem with a smooth solution. In practice, however, the immersed boundary method is often applied to problems involving an immersed elastic interface, such as a heart valve leaflet. Across such a material interface in a viscous fluid, the velocity is continuous but its normal derivatives are not. This difficulty has been overcome by a more complicated methodology known as the immersed interface method, pioneered by Zhilin Li and Randall LeVeque [21], but it has not yet been overcome within the framework of the immersed boundary method.

What then is the benefit of formal second-order accuracy? The answer has already been suggested above. This class of methods has reduced numerical viscosity and is therefore capable of improved resolution of vortex phenomena that are so important in fluid dynamics in general and in cardiac fluid dynamics in particular.

2. EQUATIONS OF MOTION

We begin by stating the equations of motion of an idealized composite material known as a fiber-reinforced fluid. This is a viscous incompressible fluid containing an immersed system of elastic fibers. The fibers are pure force generators: they contribute neither mass nor volume to the

composite, only a fiber stress, which by definition points always in the fiber direction. The fiber stress depends on the fiber strain in a possibly nonlinear, time-dependent, and spatially inhomogeneous manner. The fibers move at the local fluid velocity. Mass, volume, incompressibility, and rheological properties are all supplied by the fluid component of the composite.

For two different derivations of the equations of motion of a fiber-reinforced fluid, see [22, 23]. The notation used here will be defined after the equations have been stated. The equations are as follows:

$$\rho\left(\frac{\partial \boldsymbol{u}}{\partial t} + \boldsymbol{u}\cdot\nabla\boldsymbol{u}\right) + \nabla p = \mu\nabla^2\boldsymbol{u} + \boldsymbol{f}\,, \tag{1}$$

$$\nabla\cdot\boldsymbol{u} = 0\,, \tag{2}$$

$$\boldsymbol{f}(\boldsymbol{x},t) = \int \boldsymbol{F}(q,r,s,t)\,\delta\left(\boldsymbol{x}-\boldsymbol{X}(q,r,s,t)\right)\,\mathrm{d}q\,\mathrm{d}r\,\mathrm{d}s\,, \tag{3}$$

$$\begin{aligned}\frac{\partial \boldsymbol{X}}{\partial t}(q,r,s,t) &= \boldsymbol{u}\left(\boldsymbol{X}(q,r,s,t),t\right)\\ &= \int \boldsymbol{u}(\boldsymbol{x},t)\,\delta\left(\boldsymbol{x}-\boldsymbol{X}(q,r,s,t)\right)\,\mathrm{d}\boldsymbol{x}\,,\end{aligned} \tag{4}$$

$$\boldsymbol{F} = \frac{\partial}{\partial s}(T\boldsymbol{t})\,, \tag{5}$$

$$T = \sigma\left(\left|\frac{\partial \boldsymbol{X}}{\partial s}\right|; q,r,s,t\right)\,, \tag{6}$$

$$\boldsymbol{t} = \frac{\partial \boldsymbol{X}/\partial s}{|\partial \boldsymbol{X}/\partial s|}\,. \tag{7}$$

In this system, Eqns. $(1,2)$ are fluid equations, Eqns. (5–7) are fiber equations, and Eqns. $(3,4)$ are interaction equations. We describe the notation and meaning of each of these subsystems of equations in turn.

The fluid equations $(1,2)$ are the familiar Navier–Stokes equations of a viscous incompressible fluid. The constant parameters ρ and μ are the fluid density and viscosity, respectively. The unknown functions in the the fluid equations are the fluid velocity $\boldsymbol{u}(\boldsymbol{x},t)$, the fluid pressure $p(\boldsymbol{x},t)$, and the force per unit volume applied by the fibers to the fluid $\boldsymbol{f}(\boldsymbol{x},t)$, where $\boldsymbol{x} = (x_1,x_2,x_3)$ is the spatial position (in Cartesian coordinates), and t is the time. Note that $\boldsymbol{f}(\boldsymbol{x},t)$ is conceptually the divergence of the fiber stress tensor, but we do not make make explicit use of that stress tensor in this formulation of the equations of motion.

The fiber equations (5–7) are written in material curvilinear coordinates that are aligned with the fibers. We denote these coordinates

(q, r, s). They are chosen in such a way that fixed values of (q, r) define a particular fiber (for all time) and fixed values of (q, r, s) define a particular material point (for all time). The unknown function $\boldsymbol{X}(q, r, s, t)$ completely describes the motion of the fibers, and also their spatial configuration at any given time. For example, if we hold (q, r, s) fixed, then the equation $\boldsymbol{x} = \boldsymbol{X}(q, r, s, t)$ defines the trajectory of the material point whose coordinates are (q, r, s). On the other hand, if we hold (q, r) and t fixed but let s vary, then the same equation $\boldsymbol{x} = \boldsymbol{X}(q, r, s, t)$ defines the space curve that happens to be occupied by the fiber whose coordinates are (q, r) at the time t.

Other unknown functions of (q, r, s, t) that appear in the fiber equations are the unit tangent vector to the fibers $\boldsymbol{t}(q, r, s, t)$ (not to be confused, of course, with the scalar t, which denotes the time), the fiber tension $T(q, r, s, t)$, and the fiber force density $\boldsymbol{F}(q, r, s, t)$. More precisely, T and $\boldsymbol{F}$ are defined by the statements that the force transmitted by the bundle of fibers $\mathrm{d}q\,\mathrm{d}r$ is $\pm T\boldsymbol{t}\,\mathrm{d}q\,\mathrm{d}r$, and the force applied to the fluid by the fibers lying within the chunk of material defined by $\mathrm{d}q\,\mathrm{d}r\,\mathrm{d}s$ is $\boldsymbol{F}\,\mathrm{d}q\,\mathrm{d}r\,\mathrm{d}s$.

Taken together, the fiber equations describe how to calculate the fiber force density $\boldsymbol{F}$ from the fiber configuration $\boldsymbol{X}$ at any given time. Equation (5) relates the fiber force density $\boldsymbol{F}$ to the fiber tension T and the unit tangent $\boldsymbol{t}$. This relationship can be derived by considering the force balance on a bundle of fiber segments defined by $s_1 \le s \le s_2$, with s_1 and s_2 arbitrary, and (q, r) in some arbitrary but specified set. Recalling that the fibers are massless, and making use of the fundamental theorem of calculus, we can derive Eqn. (5). (For more detail about this derivation, see [22].) Equation (6) is the constitutive law of the fibers. It defines the fiber tension, or stress, T, as a given function σ of $|\partial\boldsymbol{X}/\partial s|$, which determines the fiber strain. Note the explicit dependence of this stress–strain relation on the material coordinates (q, r, s) and on the time t. The explicit time dependence is particularly important in the heart; it is what allows the heart muscle to contract and relax. Finally, Eqn. (7) simply defines the unit tangent $\boldsymbol{t}$ to the fibers. Since (q, r) are constant along any given fiber, the vector $\partial\boldsymbol{X}/\partial s$ is tangent to the fibers, so we need only normalize this vector to obtain the unit tangent $\boldsymbol{t}$.

Finally, we come to the interaction equations (3, 4). These both involve the three-dimensional Dirac delta function

$$\delta(\boldsymbol{x}) = \delta(x_1)\delta(x_2)\delta(x_3)\,, \tag{8}$$

which expresses the local character of the interaction. Equation (3) is a slightly nonstandard way of expressing the relationship between the two corresponding force densities $\boldsymbol{f}(\boldsymbol{x}, t)\,\mathrm{d}\boldsymbol{x}$ and $\boldsymbol{F}(q, r, s, t)\,\mathrm{d}q\,\mathrm{d}r\,\mathrm{d}s$. To

see that this is the content of Eqn. (3), integrate both sides over an arbitrary region Ω of space. On the right-hand side, interchange the order of integrations (justified by the formal character of all equations involving the delta function), and recall that $\int_\Omega \delta(\boldsymbol{x} - \boldsymbol{X})\,\mathrm{d}\boldsymbol{x}$ yields the value 1 if $\boldsymbol{X}$ is within Ω and 0 otherwise.

Equation (4) is the no-slip condition of a viscous fluid, which says, in our case, that the fibers move at the local fluid velocity. In the second form of Eqn. (4), we just make use of the defining property of the delta function to rewrite the no-slip condition in a form that resembles Eqn. (3). Then each of the interaction equations involves an integral transformation with $\delta(\boldsymbol{x} - \boldsymbol{X}(q,r,s,t))$ as kernel. In Eqn. (3), the integration is with respect to (q,r,s), so we are left with a function of $(\boldsymbol{x},t)$, but in Eqn. (4), the integration is with respect to $\boldsymbol{x}$, so we are left with a function of (q,r,s,t). A more subtle difference between these equations, though, is that the integration variable $\boldsymbol{x}$ appears directly in the argument of the delta function, whereas the integration variables (q,r,s) appear only indirectly, via the nonlinear function $\boldsymbol{X}(q,r,s,t)$. That is why the corresponding densities $\boldsymbol{F}(q,r,s,t)$ and $\boldsymbol{f}(\boldsymbol{x},t)$ do *not* have the same numerical values at corresponding points.

The distinction between $\boldsymbol{F}$ and $\boldsymbol{f}$ becomes even more significant when the fibers in question are localized on a surface, as in the case of a heart valve leaflet. One of the main strengths of the above formulation is that it can handle this case with only minor modification. If the fibers are localized on a surface, we must drop one of the curvilinear coordinates, say q. Then Eqn. (3) becomes

$$\boldsymbol{f}(\boldsymbol{x},t) = \int \boldsymbol{F}(r,s,t)\,\delta\left(\boldsymbol{x} - \boldsymbol{X}(r,s,t)\right)\,\mathrm{d}r\,\mathrm{d}s\,. \tag{9}$$

Here, $\delta(\boldsymbol{x})$ is still the three-dimensional Dirac delta function, but the integration is only over the two-dimensional surface obtained by varying (r,s). It follows that $\boldsymbol{f}(\boldsymbol{x},t)$ is singular like a one-dimensional delta function. In other words, the force per unit volume applied by a leaflet to the fluid in which it is immersed is infinite, but has the property that its integral over any finite volume is finite.

In summary, the state of our system at some fixed time t is given by the velocity field $\boldsymbol{u}(\boldsymbol{x},t)$ and by the fiber configuration $\boldsymbol{X}(q,r,s,t)$. Given the fiber configuration $\boldsymbol{X}(q,r,s,t)$, Eqns. (5–7) determine the fiber force density $\boldsymbol{F}(q,r,s,t)$ in curvilinear coordinates. Then Eqn. (3) converts this density to the fiber force density $\boldsymbol{f}(\boldsymbol{x},t)$ in Cartesian coordinates. With $\boldsymbol{f}$ known, the incompressible Navier–Stokes equations (1, 2) determine $\partial\boldsymbol{u}/\partial t$ (and p as a byproduct). Finally, Eqn. (4) determines $\partial\boldsymbol{X}/\partial t$. Thus we have, in effect, a first-order system, in which

the state of the system (in our case $(\boldsymbol{u}, \boldsymbol{X})$) determines its own rate of change $(\partial \boldsymbol{u}/\partial t, \partial \boldsymbol{X}/\partial t)$.

In applying these equations to the heart, we regard the thick muscular walls as a fiber-reinforced fluid with time-dependent elastic parameters. Here the fibers correspond to the thick (myosin) and thin (actin) filaments of cardiac muscle, and the fluid is the intracellular water. Vessel walls are modeled similarly, except that the fibers that reinforce them represent the elastin and collagen of those vessels and have time-independent elastic properties. Heart valve leaflets are modeled as fiber(collagen)-reinforced surfaces—see Eqn. (9) and the surrounding discussion. Blood in the cardiac chambers is simply governed by the Navier–Stokes equations, i.e. it is the special case of a fiber-reinforced fluid in which there are no fibers. For the tissue exterior to the heart we again use simply the Navier–Stokes equations, though one could go to the trouble to put some fibers there to model the elasticity of the external medium. Instead of this, we hold the heart loosely in place by tethering the aorta and pulmonary artery of the model to fixed locations in space by soft springs that allow recoil of the heart without letting it jet away completely. Finally we enclose the whole system in a cube with periodic boundary conditions. Since it is not practical to model the whole circulation within this cube, sources and sinks are provided to connect the veins and arteries of the model heart through hydraulic resistances to constant-pressure reservoirs. An external source/sink is also provided to allow for changes in volume of the heart during the cardiac cycle. The methodology used to handle sources and sinks is omitted from this paper to simplify the presentation.

3. NUMERICAL METHOD

We now describe a variant of the immersed boundary method with formal second-order accuracy. (See the Introduction for references and explanation of what is meant by "formal" second-order accuracy.) This is essentially a second-order Runge–Kutta method—see for example [24]. Each time step proceeds in two substeps, which we shall call the "preliminary" substep and the "final" substep. The preliminary substep proceeds from time level n to time level $n + \frac{1}{2}$ by a first-order accurate method, which in our case will be a hybrid of the forward and backward Euler method. Then the final substep starts again at time level n and proceeds directly to time level $n+1$ by a second-order accurate method, which in our case will be a hybrid of the midpoint rule and the trapezoidal rule. The data at time level $n+\frac{1}{2}$ that are needed to implement the midpoint rule are obtained from the results of the preliminary substep.

Since those data were computed by a first-order accurate method, the reader may well ask how the overall scheme can be second-order accurate. This is the magic of the Runge–Kutta methodology, which extracts higher-order results from lower-order ingredients. The basic reason why it works is that a *single time step* of a first-order accurate numerical scheme introduces errors that are only $\mathrm{O}((\Delta t)^2)$. (The first-order accuracy of the scheme manifests itself only when the scheme is used to compute over a time interval of $\mathrm{O}(1)$, which requires a large number, $\mathrm{O}((\Delta t)^{-1})$, of steps.) Thus our preliminary substep in fact produces results that are within $\mathrm{O}((\Delta t)^2)$ of the exact solution at the midpoint of the time step, and this fact allows the second-order accuracy of the final substep to be the overall accuracy of the scheme.

We use a superscript to denote the time level. Thus $\boldsymbol{X}^n(q,r,s)$ is shorthand for $\boldsymbol{X}(q,r,s,n\,\Delta t)$, where Δt is the duration of the time step, and similarly for all other variables. The given data at the beginning of the time step are $\boldsymbol{X}^n$ and $\boldsymbol{u}^n$; the goal is to compute $\boldsymbol{X}^{n+1}$ and $\boldsymbol{u}^{n+1}$.

Before describing how this is done, we have to say a few words about the spatial discretization. There are, in fact, two such discretizations: one for the fluid and one for the fibers.

The grid on which the fluid variables are defined is a fixed, uniform cubic lattice of meshwidth $h = \Delta x_1 = \Delta x_2 = \Delta x_3$. We shall make extensive use of the central difference operator D_i, defined for $i = 1, 2, 3$ as follows:

$$(\mathrm{D}_i\phi)(\boldsymbol{x}) = \frac{\phi(\boldsymbol{x} + h\boldsymbol{e}^i) - \phi(\boldsymbol{x} - h\boldsymbol{e}^i)}{2h}\,, \tag{10}$$

where $\boldsymbol{e}^i$ is the unit vector in the ith coordinate direction. As the notation suggests, D_i can be regarded as the ith component of a vector difference operator $\mathbf{D}$, in exactly the same way as $\partial/\partial x_i$ is the ith component of the vector differential operator ∇. Thus $\mathbf{D}p$ will be the discrete gradient of p, and $\mathbf{D}\cdot\boldsymbol{u}$ will be the discrete divergence of $\boldsymbol{u}$.

We shall also make use, in the viscous terms only, of a centered discrete Laplacian L, which is *not* the same as $\mathbf{D}\cdot\mathbf{D}$, the distinction being that the stencil of L is half as wide as the stencil of $\mathbf{D}\cdot\mathbf{D}$. This "tight" discrete Laplacian is defined as follows:

$$(\mathrm{L}\phi)(\boldsymbol{x}) = \sum_{i=1}^{3} \frac{\phi(\boldsymbol{x} + h\boldsymbol{e}^i) + \phi(\boldsymbol{x} - h\boldsymbol{e}^i) - 2\phi(\boldsymbol{x})}{h^2}\,. \tag{11}$$

The fiber variables are defined on a fixed rectangular lattice in (q,r,s) space with meshwidths Δq, Δr, and Δs, respectively. Note, however, that this fixed rectangular lattice in (q,r,s) space defines a moving curvilinear lattice in the physical space. Along each fiber, i.e. in the s direction, it is natural to stagger the variables in the following way: We define

the position variable $\boldsymbol{X}$ and the force density $\boldsymbol{F}$ only at values of s that are integer multiples of Δs, but we define the fiber tension T and the unit tangent to the fibers $\boldsymbol{t}$ only at "half-integer" multiples of Δs, i.e. at $s = (k+\frac{1}{2})\Delta s$, where k is an integer. These staggered data are connected by a central difference operator $\mathcal{D}_s$ defined as follows:

$$(\mathcal{D}_s\phi)(q,r,s) = \frac{\phi\left(q,r,s+\frac{1}{2}\Delta s\right) - \phi\left(q,r,s-\frac{1}{2}\Delta s\right)}{\Delta s}\,. \tag{12}$$

The fluid mesh and the fiber mesh defined above are connected by a smoothed approximation to the Dirac delta function. It is denoted δ_h and is of the following form:

$$\delta_h(\boldsymbol{x}) = \frac{1}{h^3}\phi\left(\frac{x_1}{h}\right)\phi\left(\frac{x_2}{h}\right)\phi\left(\frac{x_3}{h}\right)\,, \tag{13}$$

where $\boldsymbol{x} = (x_1, x_2, x_3)$, and where the function ϕ is determined by the following conditions:

1 ϕ is a continuous function.

2 $\phi(r) = 0$ for $|r| \geq 2$.

3 For all r, $\sum_{j \text{ even}} \phi(r-j) = \sum_{j \text{ odd}} \phi(r-j) = \frac{1}{2}$.

4 For all r, $\sum_j (r-j)\phi(r-j) = 0$.

5 For all r, $\sum_j \left(\phi(r-j)\right)^2 = C$, where C is a numerical constant, independent of r.

The motivation for these postulates is discussed in [2]. It follows (exercise for the reader!) that $C = \frac{3}{8}$ and that ϕ is given by

$$\phi(r) = \begin{cases} \dfrac{3 - 2|r| + \sqrt{1 + 4|r| - 4r^2}}{8}\,, & |r| \leq 1\,, \\ \dfrac{5 - 2|r| - \sqrt{-7 + 12|r| - 4r^2}}{8}\,, & 1 \leq |r| \leq 2\,, \\ 0\,, & 2 \leq |r|\,. \end{cases} \tag{14}$$

This is an even, bell-shaped function, which not only is continuous but has a continuous first derivative. The construction of δ_h is now complete.

We are now ready to describe a typical timestep of the numerical scheme. The preliminary substep, which goes from time level n to $n+\frac{1}{2}$, proceeds as follows:

First, we update the position of the fiber points $\boldsymbol{X}^{n+\frac{1}{2}}(q,r,s)$:

$$\frac{\boldsymbol{X}^{n+\frac{1}{2}}-\boldsymbol{X}^{n}}{\Delta t/2}=\sum_{\boldsymbol{x}}\boldsymbol{u}^{n}(\boldsymbol{x})\delta_h\left(\boldsymbol{x}-\boldsymbol{X}^{n}(q,r,s)\right)h^3\,, \tag{15}$$

which is a discretization of Eqn. (4). Here and throughout the paper $\sum_{\boldsymbol{x}}$ denotes the sum over the cubic lattice in physical space on which the fluid variables are defined. Similarly, $\sum_{q,r,s}$ will denote the sum over the rectangular lattice in (q,r,s) space on which the fiber positions $\boldsymbol{X}$ and force densities $\boldsymbol{F}$ are defined.

Next, we calculate the fiber force density $\boldsymbol{F}^{n+\frac{1}{2}}$ associated with the fiber configuration $\boldsymbol{X}^{n+\frac{1}{2}}$ as follows. First we evaluate the fiber tensions and unit tangents (at the half-integer multiples of Δs where these quantities are defined):

$$T^{n+\frac{1}{2}}=\sigma^{n+\frac{1}{2}}\left(\left|\mathcal{D}_s\boldsymbol{X}^{n+\frac{1}{2}}\right|;q,r,s\right)\,, \tag{16}$$

$$\boldsymbol{t}^{n+\frac{1}{2}}=\frac{\mathcal{D}_s\boldsymbol{X}^{n+\frac{1}{2}}}{\left|\mathcal{D}_s\boldsymbol{X}^{n+\frac{1}{2}}\right|}\,. \tag{17}$$

These are discretizations of Eqns. (6) and (7). Next, we use these results to evaluate the fiber force density $\boldsymbol{F}^{n+\frac{1}{2}}$ from the discretization of Eqn. (5):

$$\boldsymbol{F}^{n+\frac{1}{2}}=\mathcal{D}_s\left(T^{n+\frac{1}{2}}\boldsymbol{t}^{n+\frac{1}{2}}\right)\,. \tag{18}$$

The next step is to convert the fiber force density from curvilinear to Cartesian coordinates. This is done by a discretization of Eqn. (3):

$$\boldsymbol{f}^{n+\frac{1}{2}}(\boldsymbol{x})=\sum_{q,r,s}\boldsymbol{F}^{n+\frac{1}{2}}(q,r,s)\,\delta_h\left(\boldsymbol{x}-\boldsymbol{X}^{n+\frac{1}{2}}(q,r,s)\right)\,\Delta q\,\Delta r\,\Delta s\,. \tag{19}$$

With $\boldsymbol{f}^{n+\frac{1}{2}}$ in hand, we are now ready to tackle the Navier–Stokes equations. The method we use to reach the time level $n+\frac{1}{2}$ in the preliminary substep is essentially the backward Euler method, except that the nonlinear terms are treated explicitly (forward Euler). The system of equations that we have to solve is as follows:

$$\begin{aligned}\rho\left[\frac{u_i^{n+\frac{1}{2}}-u_i^{n}}{\Delta t/2}+\frac{1}{2}\left(\boldsymbol{u}\cdot\mathbf{D}u_i+\mathbf{D}\cdot(\boldsymbol{u}u_i)\right)^n\right]+\mathrm{D}_i\tilde{p}^{n+\frac{1}{2}}\\ =\mu\mathrm{L}u_i^{n+\frac{1}{2}}+f_i^{n+\frac{1}{2}}\end{aligned} \tag{20}$$

for $i = 1, 2, 3$, and

$$\mathbf{D} \cdot \boldsymbol{u}^{n+\frac{1}{2}} = 0\,. \tag{21}$$

Note that we use skew-symmetric differencing of the nonlinear terms. That is, instead of discretizing $\boldsymbol{u} \cdot \nabla u_i$ directly, we discretize instead the equivalent (because $\nabla \cdot \boldsymbol{u} = 0$) expression $\frac{1}{2}\left(\boldsymbol{u} \cdot \nabla u_i + \nabla \cdot (\boldsymbol{u} u_i)\right)$. This form is used both here in the preliminary substep and later in the final substep, but it is here evaluated at time level n, and in the final substep it will be evaluated at time level $n + \frac{1}{2}$.

The unknowns in Eqns. (20, 21) are $u_i^{n+\frac{1}{2}}(\boldsymbol{x})$ and $\tilde{p}^{n+\frac{1}{2}}(\boldsymbol{x})$, and they enter into these equations linearly and with constant coefficients. The system of equations (20, 21) can therefore be solved by fast Fourier transform—see [2] for details. This completes the preliminary substep.

The final substep is simpler than the preliminary substep because we already have the fiber forces at the time level $n + \frac{1}{2}$ and do not need to recompute them. First we use the fluid velocity $\boldsymbol{u}^{n+\frac{1}{2}}$ that we have just computed to find the fiber configuration $\boldsymbol{X}^{n+1}$ at the end of the timestep:

$$\frac{\boldsymbol{X}^{n+1} - \boldsymbol{X}^n}{\Delta t} = \sum_{\boldsymbol{x}} \boldsymbol{u}^{n+\frac{1}{2}}(\boldsymbol{x}) \delta_h \left(\boldsymbol{x} - \boldsymbol{X}^{n+\frac{1}{2}}(q, r, s)\right) h^3\,. \tag{22}$$

Note that this is an implementation of the midpoint rule.

The last thing that we have to do is to find the fluid velocity $\boldsymbol{u}^{n+1}$ at the end of the time step. This is done by solving the following system in the unknowns $u_i^{n+1}(\boldsymbol{x})$ and $p^{n+\frac{1}{2}}(\boldsymbol{x})$:

$$\begin{aligned} \rho \left[\frac{u_i^{n+1} - u_i^n}{\Delta t} + \frac{1}{2} \left(\boldsymbol{u} \cdot \mathbf{D} u_i + \mathbf{D} \cdot (\boldsymbol{u} u_i)\right)^{n+\frac{1}{2}} \right] + \mathrm{D}_i p^{n+\frac{1}{2}} \\ = \tfrac{1}{2}\mu \mathrm{L}\left(u_i^n + u_i^{n+1}\right) + f_i^{n+\frac{1}{2}} \end{aligned} \tag{23}$$

for $i = 1, 2, 3$, and

$$\mathbf{D} \cdot \boldsymbol{u}^{n+1} = 0\,. \tag{24}$$

(Note the distinction between $p^{n+\frac{1}{2}}$ and $\tilde{p}^{n+\frac{1}{2}}$, which appeared above. They are two different approximations to the pressure at time level $n+\frac{1}{2}$.) Here we have a mixture of the midpoint rule (for the nonlinear pressure gradient and fiber force terms) and the trapezoidal rule (for the viscous terms). Although Eqn. (24) does not appear to be centered in time, it actually holds for all n and therefore implies that $\mathbf{D} \cdot \boldsymbol{u}^n = 0$, also. Thus, the condition that the discrete divergence of the velocity should vanish does indeed hold in a symmetrical way at both the beginning and end of the timestep (and in the middle, too—see Eqn. (21)). The system of

Eqns. (23, 24) is very similar to Eqns. (20, 21), and it is straightforward to write a single subroutine based on the fast Fourier transform that can be used to solve either of them. Since we have now computed $\boldsymbol{X}^{n+1}$ and $\boldsymbol{u}^{n+1}$, the timestep is complete.

4. RESULTS

The equations and numerical method described above have been used in computer simulations of the heart. For details concerning the construction of the heart model, see [2, 25]. The parameters are those of the human heart. In particular, the viscosity is that of blood, and the Reynolds number is physiological. (This is in contrast to earlier work where the viscosity was artificially elevated for numerical reasons.) The benchmark studies cited in the Introduction give reason to believe that the physical viscosity is not dominated by numerical viscosity in the computational results shown here.

We show two types of figure in the following. One type is intended to show flow in terms of streamlines. The streamlines are obtained by choosing a time of interest, fixing the velocity field at that given time, and then computing and plotting what the trajectories of selected fluid particles would be if the particles were to move in that (time-independent) velocity field. In this way we construct curves that are everywhere tangent to the fluid velocity field at the chosen time, and thus indicate the spatial direction of flow at each point (except for sign, which is usually clear from context). The density of the computed streamlines has no particular significance and depends on the arbitrary placement of the selected fluid particles. Note that streamlines cross boundaries because the boundaries are in motion. This is a fundamental feature of flow with moving boundaries, and it makes the flow geometry quite different from what it would be if the boundaries were fixed in place. Finally, we take a thin (but not infinitely thin) section through the heart model at the chosen time, and plot whatever parts of the heart model and of the streamlines that happen to lie within that section. This is most effective if the plane of the section is approximately parallel to the flow.

The other type of figure is intended to show structure only, and we use it here to convey the structure of the heart valves of the model. For this purpose we use a perspective view showing the fibers that comprise the model valves.

Figure 1 shows a section through the model left ventricle during ventricular diastole (relaxation). Flow through the open mitral valve fills the left ventricle, and the closed aortic valve prevents backflow from the

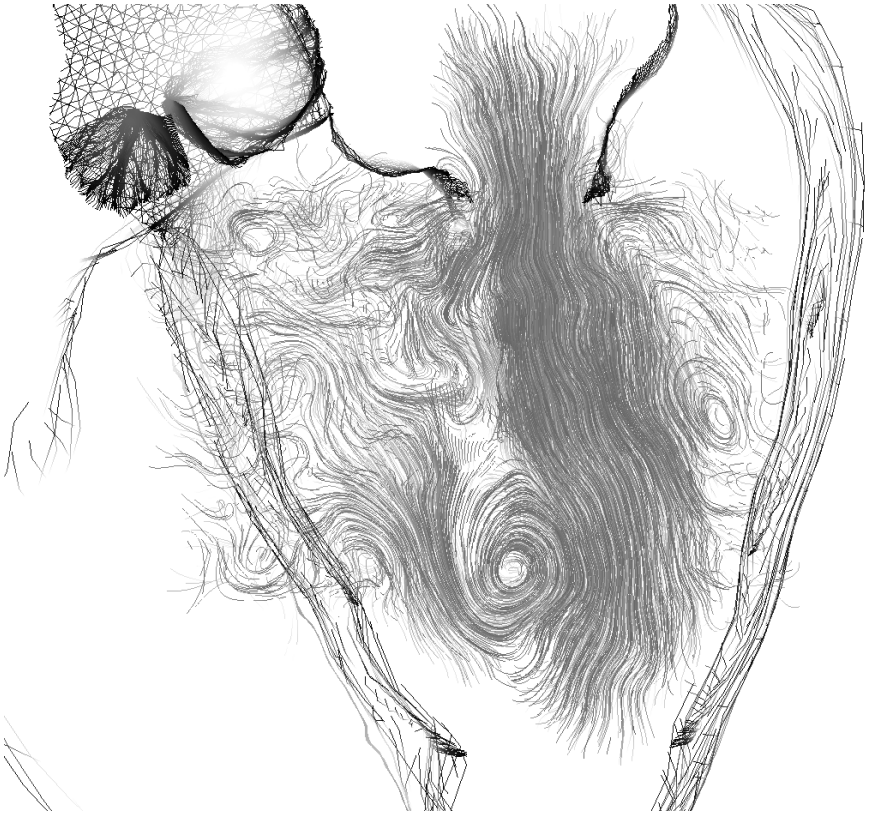

Figure 1 Section through the model left ventricle showing streamlines of ventricular filling. The closed aortic valve is at the top, left side of the figure, and the open mitral valve is at the top right. A pair of vortices (cross-section of a vortex ring) has been shed from the mitral leaflets and has migrated downwards towards the apex of the left ventricle.

aorta. Note the vortex pair (actually, the cross section of a ring vortex) that was shed from the mitral valve and has since migrated most of the way down towards the apex of the left ventricle. For a perspective view of the open mitral valve, see Figure 2.

Figure 3 shows a cross section through the axis of the aorta, bisecting one leaflet of the three-leaflet aortic valve. Behind that leaflet, a prominent vortex is seen in the aortic sinus. This is the first time we have been able to resolve an aortic sinus vortex; presumably we can do so now because of the improved accuracy associated with the numerical scheme described earlier. For a more detailed view of the structure of the aortic and pulmonic valves of the model, see Fig. 4.

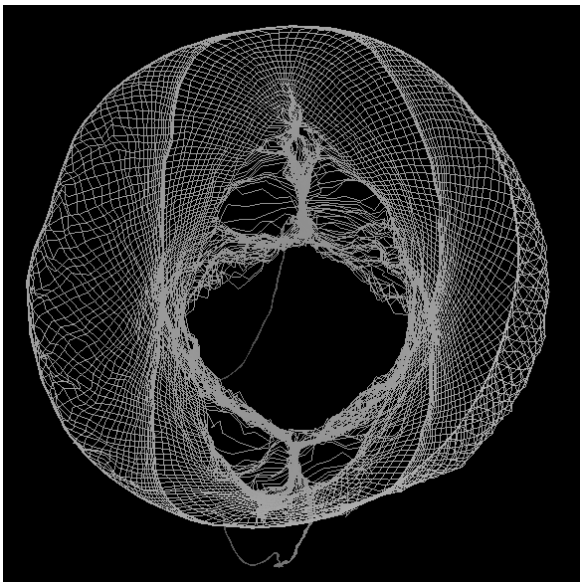

Figure 2 Perspective view of the open mitral valve, seen from the left atrium looking downwards into the left ventricle.

5. SUMMARY AND CONCLUSIONS

We have stated the equations of motion of a fiber-reinforced fluid and have indicated how those equations may be used to obtain a unified mathematical model of cardiac mechanics, including both the fluid dynamics of blood in the cardiac chambers and also the contractility of the cardiac muscle and the elasticity of the heart valve leaflets. We have also described an immersed boundary method with formal second-order accuracy that can be used to solve the equations of this heart model. Although this method is actually second-order accurate only when it is applied to problems with smooth solutions, it nevertheless is useful for problems with non-smooth solutions because of its reduced numerical viscosity, which allows better resolution of the vortices that are shed from the heart valve leaflets.

Acknowledgments

We thank the organizers of ICTAM 2000 for this splendid opportunity to present our work to the theoretical and applied mechanics community. We also thank the National Science Foundation (USA) for support of this work under KDI research grant DMS-9980069. Computation was performed on the Cray T-90 computer at the San Diego Supercomputer Center under an allocation of resources MCA93S004P from the National Resource Allocation Committee.

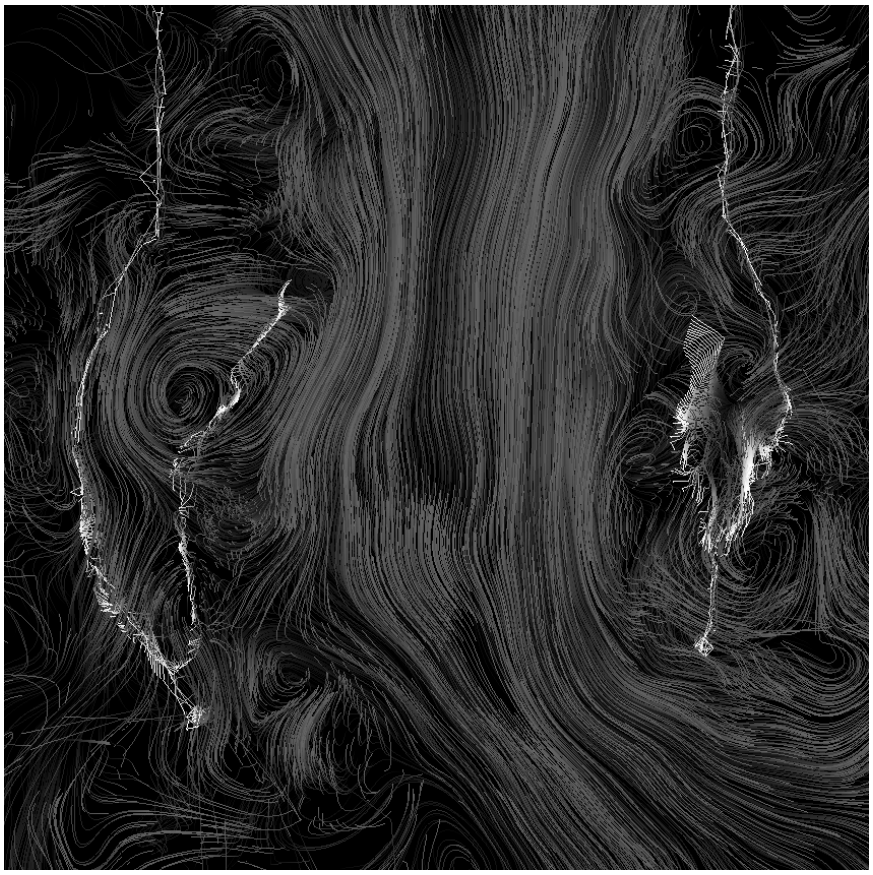

Figure 3 Section containing the axis of the ascending aorta and approximately bisecting one leaflet of the aortic valve (the one on the left in the figure). A prominent vortex appears in the sinus behind this leaflet.

References

[1] Peskin, C. S. 1972. Flow patterns around heart valves: A digital computer method for solving the equations of motion. Ph.D. thesis, Albert Einstein College of Medicine, 211 pp. (available at http://www.umi.com/hp/Products/DisExpress.html, order number 7230378).

[2] Peskin, C. S., and D. M. McQueen. 1996. Fluid dynamics of the heart and its valves. In *Case Studies in Mathematical Modeling: Ecology, Physiology, and Cell Biology* (H. G. Othmer, F. R. Adler, M. A. Lewis, and J. C. Dallon, eds.). Englewood Cliffs, N.J.: Prentice-Hall, 309–337.

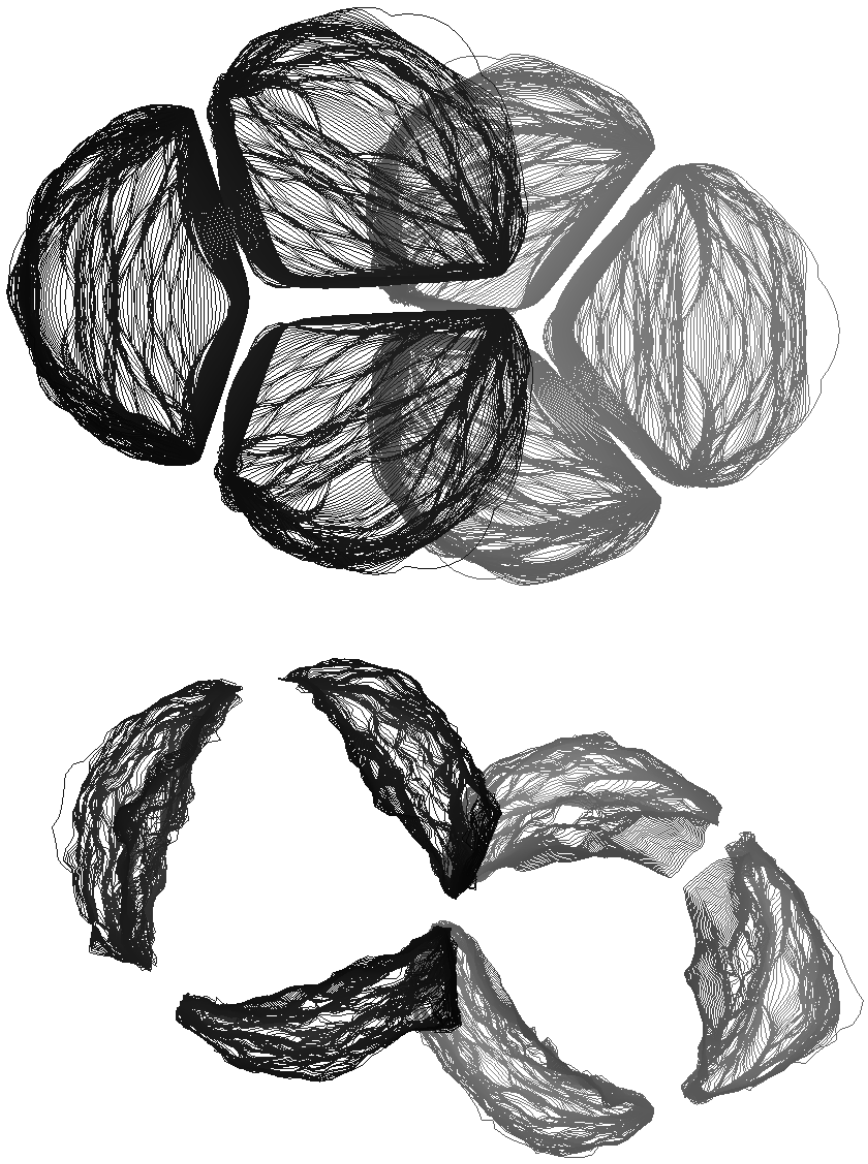

Figure 4 The aortic and pulmonic valves viewed from the arterial side looking towards the ventricles. The closed valves are shown at the top and the open valves at the bottom of the figure. The pulmonic valve (left side of the figure) appears darker because it is closer to the observer (depth cueing).

[3] McQueen, D. M., and C. S. Peskin. 1997. Shared-memory parallel vector implementation of the immersed boundary method for the

computation of blood flow in the beating mammalian heart. *Journal of Supercomputing* **11**(3), 213–236.

[4] McQueen, D. M., and C. S. Peskin. 1983. Computer-assisted design of pivoting-disc prosthetic mitral valves. *Journal of Thoracic and Cardiovascular Surgery* **86**, 126–135.

[5] McQueen, D. M., and C. S. Peskin. 1985. Computer-assisted design of butterfly bileaflet valves for the mitral position. *Scandinavian Journal of Thoracic and Cardiovascular Surgery* **19**, 139–148.

[6] McQueen, D. M., and C. S. Peskin. June 25, 1991. Curved butterfly bileaflet prosthetic cardiac valve. U.S. patent number 5,026,391.

[7] Fogelson, A. L. 1984. A mathematical model and numerical method for studying platelet adhesion and aggregation during blood clotting. *Journal of Computational Physics* **56**, 111–134.

[8] Fauci, L. J., and C. S. Peskin. 1988. A computational model of aquatic animal locomotion. *Journal of Computational Physics* **77**, 85–108.

[9] Fauci, L. J., and A. L. Fogelson. 1993. Truncated Newton methods and the modeling of complex immersed elastic structures. *Communications in Pure and Applied Mathematics* **46**, 787–818.

[10] Beyer, R. P. 1992. A computational model of the cochlea using the immersed boundary method. *Journal of Computational Physics* **98**, 145–162.

[11] Fauci, L. J., and A. McDonald. 1995. Sperm motility in the presence of boundaries. *Bulletin of Mathematical Biology* **57**, 679–699.

[12] Givelberg, E. 1997. Modeling elastic shells immersed in fluid. Ph.D. thesis, Mathematics, New York University (available at http://www.umi.com/hp/Products/DisExpress.html, order number 9808292).

[13] Eggleton, C. D., and A. S. Popel. 1998. Large deformation of red blood cell ghosts in a simple shear flow. *Physics of Fluids* **10**, 1834–1845.

[14] Arthurs, K. M., L. C. Moore, C. S. Peskin, E. B. Pitman, and H. E. Layton. 1998. Modeling arteriolar flow and mass transport using the immersed boundary method. *Journal of Computational Physics* **147**, 402–440.

[15] Bottino, D. C. 1998. Modeling viscoelastic networks and cell deformation in the context of the immersed boundary method. *Journal of Computational Physics* **147**, 86–113.

[16] Stockie, J. M., and S. I. Green. 1998. Simulating the motion of flexible pulp fibres using the immersed boundary method. *Journal of Computational Physics* **147**, 147–165.

[17] Grunbaum, D., D. Eyre, and A. Fogelson. 1998. Functional geometry of ciliated tentacular arrays in active suspension feeders. *Journal of Experimental Biology* **201**, 2575–2589.

[18] Dillon, R., and L. J. Fauci. 2000. A microscale model of bacterial and biofilm dynamics in porous media. *Biotechnology and Bioengineering* **68**, 536–547.

[19] Lai, M.-C. 1998. Simulations of the flow past an array of circular cylinders as a test of the immersed boundary method. Ph.D. thesis, Mathematics, New York University, 80 pp. (available at http://www.umi.com/hp/Products/DisExpress.html, order number 9907167).

[20] Lai, M.-C., and C. S. Peskin. 2000. An immersed boundary method with formal second order accuracy and reduced numerical viscosity. *Journal of Computational Physics* **160**, 705–719.

[21] LeVeque, R. J., and Z. Li. 1997. Immersed interface methods for Stokes flow with elastic boundaries or surface tension. *SIAM Journal on Scientific Computing* **18**, 709–735.

[22] Peskin, C. S., and D. M. McQueen. 1989. A three-dimensional computational method for blood flow in the heart: (I) immersed elastic fibers in a viscous incompressible fluid. *Journal of Computational Physics* **81**, 372–405.

[23] Peskin, C. S., and D. M. McQueen. 1993. Computational biofluid dynamics. *Contemporary Mathematics* **141**, 161–186.

[24] Press, W. H., B. P. Flannery, S. A. Teukolsky, and W. T. Vetterling. 1986. *Numerical Recipes.* Cambridge: Cambridge University Press, 550–551.

[25] McQueen, D. M., and C. S. Peskin. 2000. A three-dimensional computer model of the human heart for studying cardiac fluid dynamics. *Computer Graphics* **34**, 56–60.